Jurnal Otomasi Kontrol dan Instrumentasi Vol19 (1), 2027 ISSN: 2085-2517
https://doi.org/10.5614/joki.2027.19.1.1 E-ISSN: 2460-6340

Design of Active Yaw Gaze-Locking Control for Quadcopters in Tower Orbital Inspection

Perancangan Kontrol Penguncian Tatapan Yaw Aktif pada Quadcopter untuk Inspeksi Orbital Menara

[1,2]Faqihza Mukhlish *), [2,3]Izma Alhazmi Herdian and [4]Ihsan M Fauzan

[1]Engineering Physics, Faculty of Industrial Technology, Institut Teknologi Bandung, Bandung 40132, Indonesia

[2]Center for Instrumentation Technology and Automation, Institut Teknologi Bandung, Bandung 40132, Indonesia

[3]Instrumentation and Control, Faculty of Industrial Technology, Institut Teknologi Bandung, Bandung 40132, Indonesia

[4] Robotics, College of Computing and Mathematical Sciences, Khalifa University, United Arab Emirates

*) *corresponding email: faqihza.m@itb.ac.id*

Abstract

Close-range 3D photogrammetric inspection of tall towers with quadcopters is degraded by wind, which pushes the vehicle off its scanning orbit and changes the camera-to-structure distance. Conventional flight controllers track a time-parameterized trajectory, so wind-induced lag must be corrected in both space and time. This paper presents a cascaded geometric vector field (VF) guidance law combined with active yaw gaze-locking for helical tower scanning. The VF decouples spatial convergence from timing, an outer velocity PI loop rejects wind through its integral action by tilting the vehicle into the wind, and the yaw channel is dedicated to keeping the camera pointed at the tower axis. In 6-DoF simulations with a 4.5 m/s mean wind, gusts, and Dryden turbulence, 30 paired Monte Carlo runs with PSO-tuned gains show that the VF reduces the mean cross-track error by 70.6% relative to PID trajectory tracking and by 48.3% relative to nonlinear guidance logic (NLGL), and reduces the stand-off distance variation by 65.8% ($p < 0.001$). Because the gaze-locking law uses the measured position, the camera pointing error remained about 0.8° for all guidance laws, showing that pointing accuracy is set by the yaw loop and is decoupled from path following.

Keywords: quadcopter, geometric vector field, active yaw gaze-locking, 3D photogrammetry, wind compensation

Abstrak

Inspeksi fotogrametri 3D jarak dekat pada menara tinggi menggunakan quadcopter *terganggu oleh angin yang mendorong wahana keluar dari orbit pemindaian dan mengubah jarak kamera terhadap struktur. Sistem kendali penerbangan konvensional melacak lintasan berparameter waktu, sehingga keterlambatan akibat angin harus dikoreksi secara spasial dan temporal sekaligus. Artikel ini menyajikan hukum pemandu medan vektor (*vector field*, VF) geometris bertingkat yang dipadukan dengan penguncian tatapan yaw aktif untuk pemindaian heliks pada menara. VF memisahkan konvergensi spasial dari kendala waktu, kalang luar PI kecepatan menolak gangguan angin melalui aksi integralnya dengan memiringkan wahana ke arah datangnya angin, dan kanal* yaw *khusus digunakan untuk menjaga kamera tetap mengarah ke sumbu menara. Pada simulasi 6-derajat kebebasan dengan angin rata-rata 4.5 m/s, hembusan, dan turbulensi Dryden, 30 run Monte Carlo berpasangan dengan penguat hasil tuning PSO menunjukkan bahwa VF menurunkan galat* cross-track *rata-rata sebesar 70.6% dibandingkan pelacakan lintasan PID dan 48.3% dibandingkan* nonlinear guidance logic *(NLGL), serta menurunkan variasi jarak pandang sebesar 65.8% ($p < 0.001$). Karena hukum penguncian tatapan memakai posisi terukur, galat pembidikan kamera tetap sekitar 0.8° untuk semua hukum pemandu, yang menunjukkan bahwa akurasi pembidikan ditentukan oleh kalang* yaw *dan terpisah dari pengikutan lintasan.*

Kata Kunci: quadcopter, medan vektor geometris, penguncian tatapan yaw aktif, fotogrametri, kompensasi angin

Paper submitted Augustus 14th, 2026 – paper revised October 2nd, 2026– accepted October 16th, 2026

This paper is open access with CC BY-SA *license*.

1 Introduction

Unmanned Aerial Vehicles (UAVs) have emerged as essential platforms across civil, industrial, military, and environmental sectors, performing critical tasks such as surveying, mapping, high-altitude photography, and infrastructure inspection [1],[2]. Among various UAV configurations, multirotor platforms, particularly

quadcopters, are highly preferred due to their outstanding maneuverability, ease of maintenance, vertical take-off and landing (VTOL) capabilities, and hovering capacity [1],[3]. To inspect and reconstruct high-fidelity 3D models of tall structures like towers, wind turbines, and chimneys, a quadrotor must execute close-range helical or orbital flight paths around the target while capturing dense, multi-angle visual imagery [2],[4]. Initially, quadrotor research focused heavily on stabilizing the vehicle's fast and highly unstable attitude dynamics applying Proportional-Integral-Derivative (PID) control, backstepping, sliding mode control, and adaptive control [1],[5]. While attitude stabilization has been successfully addressed through various classical and advanced control techniques, the modern challenge has shifted toward high-precision trajectory control, path planning, and robust disturbance rejection [6],[7].

The trajectory control problem is conventionally addressed through two distinct paradigms: trajectory tracking and path following [6]. In trajectory tracking, the control objective is to force the vehicle to track a pre-established path with a strict temporal schedule, where the desired references are expressed as a direct time-varying coordinate vector [3],[8]. While trajectory tracking controllers can successfully achieve target setpoints in calm conditions [8], they exhibit severe degradation when subjected to realistic environmental disturbances such as wind gusts, shear, and localized turbulence [3]. In outdoor inspection scenarios, a lightweight quadrotor is highly sensitive to wind disturbances, which cause large position deviations from the desired path [3],[5]. Under a time-dependent trajectory tracking controller, the quadcopter is forced to chase a virtual, moving temporal point. When pushed off-course by wind drift, the vehicle expends massive control authority trying to correct both spatial coordinate deviations and temporal phase lags simultaneously [6], [9]. This often leads to actuator saturation, persistent tracking oscillations, and severe elliptical deformation of the scanning orbit [6],[10]. For 3D photogrammetric reconstruction, such tracking drift and oscillations are highly detrimental, as they cause motion blur, target clipping, and incomplete coverage of the scanned structure [2],[4]. Hence, a solid gaze alignment ensuring perfect overlapping frames is critical for high-fidelity 3D structural reconstruction [11].

To eliminate the limitations of temporal scheduling, modern research has shifted toward time-independent path-following (PF) control [6]. The PF framework removes timing constraints from the control loop, allowing the controller to prioritize spatial convergence to the path manifold over speed tracking [6],[11]. Among various path-following techniques, Vector Field (VF) guidance has emerged as an elegant and computationally efficient methodology [11],[12]. In a VF-based system, a set of virtual guidance vectors is placed around the desired path, commanding course inputs to the autopilot to guide the vehicle asymptotically toward the path perimeter [11],[13]. When integrated with a cascaded inner velocity loop, the integral action of the velocity controller acts as an active wind-drift estimator, allowing the vehicle to naturally crab into the crosswind and maintain path convergence with minimal control effort [12],[13],[14]. Furthermore, 3D circumnavigation control strategies have been developed to loiter or circle targets, transforming the orbital tracking task into a velocity tracking problem that can be stabilized using robust sliding mode or adaptive methods [15],[16]. Despite these advancements, integrating geometric vector field guidance with active camera pointing (gaze-locking) for high-precision 3D vertical reconstruction remains an open challenge [17],[18],[19].

Combining path following with camera pointing is not new in itself. For fixed-wing UAVs, Rysdyk [20] derived wind-corrected orbit geometries that keep a ground target at a constant line-of-sight angle in the body frame, and Frew et al. [21] used Lyapunov guidance vector fields for standoff tracking of moving targets; a comparative analysis of the underlying path-following laws is given in [22]. In these works the aircraft heading is tied to its course, so the camera line of sight can only be held by reshaping the orbit or by a gimbal. A multirotor does not share this constraint, because its yaw can be commanded independently of its ground course. The contribution of this paper is therefore an engineering integration rather than a new control law: we (i) assign wind rejection entirely to the roll–pitch channel through the integral action of the outer velocity loop and dedicate the yaw channel to gaze-locking, (ii) provide a convergence analysis of the resulting vector-field and velocity-loop structure, and (iii) quantify, over randomized wind realizations and against two baselines, how wind-induced path error propagates into photogrammetric quality metrics such as stand-off distance variation and image-plane target offset.

In this research, we address this critical gap by developing and formulating a Cascaded Geometric Vector Field (VF) Guidance Control System coupled with an Active Yaw Gaze-Locking algorithm for quadcopter-based tall structure scanning under high-wind conditions. The main contribution of this paper is the integration of a time-independent 3D helical path-following manifold with an outer-loop velocity PI controller and an active camera gaze-lock. This architecture allows the quadcopter to maintain a precise, circular orbit around a tall tower while actively compensating for wind drift through coordinated crab maneuvers, while the yaw channel keeps the camera pointed at the tower axis. The explicit objective of this study is to mathematically formulate this hierarchical control system, implement it in a continuous-time simulation platform, and conduct a comparative performance evaluation against standard time-dependent PID trajectory tracking and the nonlinear guidance logic (NLGL) of [23] under identical wind realizations. By showing that the VF-guidance approach reduces

cross-track error and stand-off distance variation while camera pointing is maintained by the decoupled yaw loop, this work provides a control framework for high-precision autonomous UAV photogrammetry in windy environments.

2 Method

The development of the robust high-altitude scanning system relies on a rigorous mathematical framework mapping high-level geometric guidance command to low-level motor actuator inputs. This section details the complete 6-DoF quadcopter equations of motion, the cascaded attitude and velocity tracking controllers, the guidance laws (parametric helical tracking, geometric vector field, and the NLGL baseline) with a convergence analysis of the vector field, the active target gaze-locking algorithm and camera model, and the aerodynamic disturbance model.

2.1 6-DoF Quadcopter Kinematics and Dynamics

To describe the translational and rotational motion of the quadrotor, two principal coordinate systems are defined. First, the inertial world frame $W = \{X_W, Y_W, Z_W\}$, which is fixed to the earth with Z_W pointing upwards against gravity, the X-axis pointing East, and the Y-axis pointing North (East–North–Up convention). And second, body-fixed frame $B = \{X_B, Y_B, Z_B\}$, where the origin O_B coincides with the quadcopter's center of mass (CoM). The X_B axis points toward the quadcopter's forward direction, Y_B to the left, and Z_B upwards normal to the rotor plane. Lastly, rotation matrix r_{WB} translates body frame movements into inertia movement, see Figure 1.

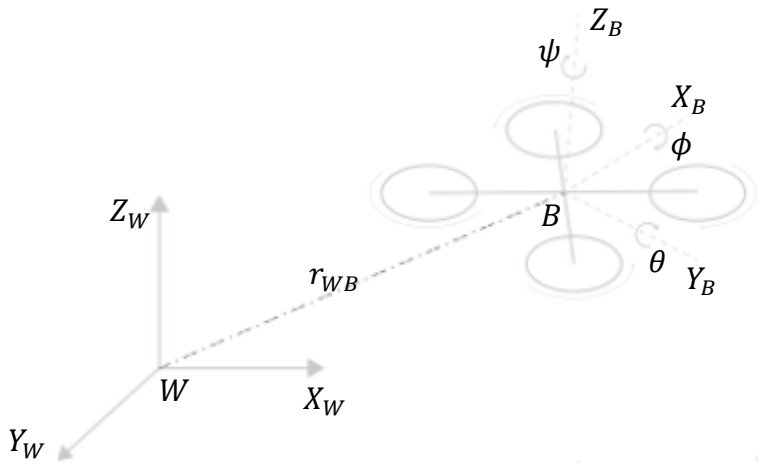


Figure 1. Quadrotor coordinate system

Let the absolute spatial position and translational velocities of the quadrotor in W be denoted by $\boldsymbol{p} = [x, y, z]^T$ and $\boldsymbol{v} = [\dot{x}, \dot{y}, \dot{z}]^T$, respectively. The orientation (attitude) is defined by Euler angles $\boldsymbol{\eta} = [\phi, \theta, \psi]^T$ corresponding to roll, pitch, and yaw, respectively. Under small-angle assumptions around hover conditions, the angular rates in the body frame $\boldsymbol{\omega} = [p, q, r]^T$ are assumed satisfy $\dot{\phi}, \dot{\theta}, \dot{\psi} \approx (p, q, r)$.

Using the Newton-Euler rigid-body formulation, the 6-DoF equations of motion are formulated as follows:

$$\ddot{x} = \frac{U_1}{m}(\cos\phi \sin\theta \cos\psi + \sin\phi \sin\psi) - \frac{F_{drag,x}}{m} \tag{1}$$

$$\ddot{y} = \frac{U_1}{m}(\cos\phi \sin\theta \sin\psi - \sin\phi \cos\psi) - \frac{F_{drag,y}}{m} \tag{2}$$

$$\ddot{z} = \frac{U_1}{m}(\cos\phi \cos\theta) - g - \frac{F_{drag,z}}{m} \tag{3}$$

$$\ddot{\phi} = \frac{I_y - I_z}{I_x}\dot{\theta}\dot{\psi} - \frac{J_r}{I_x}\dot{\theta}\Omega_r + \frac{U_2}{I_x} \tag{4}$$

$$\ddot{\theta} = \frac{I_z - I_x}{I_y}\dot{\phi}\dot{\psi} + \frac{J_r}{I_y}\dot{\phi}\Omega_r + \frac{U_3}{I_y} \tag{5}$$

$$\ddot{\psi} = \frac{I_x - I_y}{I_z}\dot{\phi}\dot{\theta} + \frac{U_4}{I_z} \tag{6}$$

Where m is the total mass of the quadrotor, g is the acceleration due to gravity, I_x, I_y, I_z represent the principal moments of inertia along the body axes, J_r is the rotor moment of inertia, and $\Omega_r = -\Omega_1 + \Omega_2 - \Omega_3 + \Omega_4$ is the residual motor spin speed. Then, F_{drag} represents the aerodynamics drag force vector. And lastly, U_1, U_2, U_3, U_4 are the primary control inputs: total vertical thrust, roll torque, pitch torque, and yaw torque, respectively.

These control variables are mapped to the physical motor speeds (Ω_i) using the rotor thrust (b) and drag (d) coefficients, with arm length l, as result:

$$\begin{bmatrix} U_1 \\ U_2 \\ U_3 \\ U_4 \end{bmatrix} = \begin{bmatrix} b & b & b & b \\ 0 & -bl & 0 & bl \\ -bl & 0 & bl & 0 \\ d & -d & d & -d \end{bmatrix} \begin{bmatrix} \Omega_1^2 \\ \Omega_2^2 \\ \Omega_3^2 \\ \Omega_4^2 \end{bmatrix} \tag{7}$$

At every control step the mixer (7) is inverted to obtain the squared motor speeds, which are saturated to $[0, \Omega_{max}^2]$; the yaw torque has the lowest priority and only uses the remaining motor headroom. The vehicle parameters used in the simulation are $m = 1.5$ kg, $I_x = I_y = 0.011$ kg·m², $I_z = 0.022$ kg·m², $J_r = 6 \times 10^{-5}$ kg·m², $l = 0.23$ m, $b = 1.0 \times 10^{-5}$ N·s², $d = 2.4 \times 10^{-7}$ N·m·s², and a thrust-to-weight ratio of 2, which give hover and maximum motor speeds of 607 rad/s and 858 rad/s.

2.2 Cascaded Control Loop Design

The highly non-linear, underactuated dynamics of the quadrotor are stabilized by separating the controller into a fast inner loop (attitude and rate stabilization) and a slower outer loop (translational tracking). Depending on the selected guidance algorithm, two distinct outer horizontal control structures are formulated to compute the virtual acceleration demands $(u_{x,acc}, u_{y,acc})$.

2.2.1 Inner-Loop Attitude and Altitude Stabilization

The inner loop operates at as high frequency (500 Hz) to track the desired roll, pitch, yaw angles, and the vertical altitude. Since the desired angles are constant and with hovering assumption $\dot{\phi}, \dot{\theta}, \dot{\psi} \approx (p, q, r)$, the error derivative $\dot{e}_\phi(t) = \dot{\phi}_d - \dot{\phi}(t)$ can be simplified as $\dot{e}_\phi(t) = -p(t)$. Hence the Proportional-Integral-Derivative (PID) control laws are formulated as:

$$U_1 = K_{Pz}e_z(t) + K_{Iz}\int_0^t e_z(\tau)\,d\tau + K_{Dz}\dot{e}_z(t) + mg \tag{8}$$

$$U_2 = K_{P\phi}e_\phi(t) + K_{I\phi}\int_0^t e_\phi(\tau)\,d\tau - K_{D\phi}p(t) \tag{9}$$

$$U_3 = K_{P\theta}e_\theta(t) + K_{I\theta}\int_0^t e_\theta(\tau)\,d\tau - K_{D\theta}q(t) \tag{10}$$

$$U_4 = K_{P\psi}e_\psi(t) + K_{I\psi}\int_0^t e_\psi(\tau)\,d\tau - K_{D\psi}r(t) \tag{11}$$

With $K_{Pz}, K_{P\phi}, K_{P\theta}, K_{P\psi}$ are proportional gains for altitude, roll, pitch, and yaw errors. $K_{Iz}, K_{I\phi}, K_{I\theta}, K_{I\psi}$ are integral gains for altitude, roll, pitch, and yaw sum of errors. And $K_{Dz}, K_{D\phi}, K_{D\theta}, K_{D\psi}$ are derivative gains for altitude and angular rates. $p(t), q(t), r(t)$ are the angular rate gyroscope measurements.

The tracking error terms ($e_z, e_\phi, e_\theta, e_\psi$) are defined as:

$$e_z(t) = z_d(t) - z(t) \tag{12}$$

$$e_{\phi}(t) = \phi_d(t) - \phi(t) \tag{13}$$

$$e_{\theta}(t) = \theta_d(t) - \theta(t) \tag{14}$$

$$e_{\psi}(t) = \psi_d(t) - \psi(t) \tag{15}$$

2.2.2 Outer-Loop 1: Position PID Controller (Trajectory Tracking Configuration)

For the baseline standard trajectory tracking system, lateral translation is governed by a direct position-tracking PID controller with derivative velocity feedback. This loop computes the virtual horizontal acceleration demands directly from position and velocity errors:

$$u_{xacc} = K_{Ppos}e_x(t) + K_{Ipos}\int_0^t e_x(\tau)\,d\tau + K_{Dpos}(v_{xd} - v_x) \tag{16}$$

$$u_{yacc} = K_{Ppos}e_y(t) + K_{Ipos}\int_0^t e_y(\tau)\,d\tau + K_{Dpos}\left(v_{yd} - v_y\right) \tag{17}$$

Where, K_{Ppos}, K_{Ipos} and K_{Dpos} are the proportional, integral, and derivative gains for the position error, and the position error terms are

$$e_x(t) = x_d(t) - x(t) \tag{18}$$

$$e_y(t) = y_d(t) - y(t) \tag{19}$$

$$\dot{e}_x = \dot{x}_d - \dot{x} = v_{xd} - v_x \tag{20}$$

$$\dot{e}_y = \dot{y}_d - \dot{y} = v_{yd} - v_y \tag{21}$$

With v_{xd} and v_{yd} are desired velocities generated by guidance laws.

2.2.3 Outer-Loop 2: Velocity PI Controller (Vector Field Path-Following Configuration)

For the proposed Geometric Vector Field path-following system, the spatial guidance law directly outputs desired ground velocity references $\left(v_{xd}, v_{yd}\right)$ rather than coordinates. To track these references, a dedicated velocity PI loop is utilized:

$$u_{xacc} = K_{Pv}(v_{xd} - v_x) + K_{Iv}\int_0^t (v_{xd} - v_x)\,d\tau \tag{22}$$

$$u_{yacc} = K_{Pv}\left(v_{yd} - v_y\right) + K_{Iv}\int_0^t \left(v_{yd} - v_y\right)d\tau \tag{23}$$

Under constant crosswinds, the velocity error integral terms act as a passive aerodynamic force estimator. They steadily accumulate to generate pitch and roll tilt demands, forcing the quadrotor to adopt a constant "crab angle" into the wind to maintain the desired trajectory.

2.2.4 Virtual Acceleration to Attitude Angle Mapping

Regardless of which outer-loop controller configuration is used to compute u_{xacc} and u_{yacc}, these virtual forces are translated to physical desired roll ϕ_d and pitch θ_d angles using the current yaw orientation ψ:

$$\phi_d = \frac{1}{g}\left(u_{xacc}\sin(\psi) - u_{yacc}\cos(\psi)\right) \tag{24}$$

$$\theta_d = \frac{1}{g}\left(u_{xacc}\cos(\psi) + u_{yacc}\sin(\psi)\right) \tag{25}$$

To ensure flight safety, small-angle approximation validity, and prevent altitude thrust loss, these commands are bounded to a maximum angle of 25^o $(0.43\ \text{rad})$:

$$\phi_{d,clamped} = \text{clip}(\phi_d, -0.43, 0.43), \qquad \theta_{d,clamped} = \text{clip}(\theta_d, -0.43, 0.43)$$

2.3 Guidance Laws and Orbit Generation

To achieve close-range vertical scans of tall objects, three high-level guidance laws are evaluated: the time-parameterized trajectory used as the conventional baseline, the proposed geometric vector field, and the NLGL as a baseline from the literature.

2.3.1 Parametric Helical Trajectory Tracking

In PID position control for trajectory tracking, the high-level mission control commands time-dependent spatial coordinates:

$$x_d(t) = x_t + R\cos(\omega_0 t) \tag{26}$$

$$y_d(t) = y_t + R\sin(\omega_0 t) \tag{27}$$

$$z_d(t) = z_{\text{start}} + v_z t \tag{28}$$

Where (x_t, y_t) is the center of the tower, R is the scanning radius $(10\ m)$, ω_0 is the orbital velocity $(0.15\ rad/s)$, and v_z is the slow climbing rate $(0.4\ m/s)$.

The reference velocities serve directly as derivative feedforward terms in the standard position tracking loop:

$$v_{x,d}(t) = -R\omega_0 \sin(\omega_0 t) \tag{29}$$

$$v_{y,d}(t) = R\omega_0 \cos(\omega_0 t) \tag{30}$$

2.3.2 Geometric Vector Field (VF) Path Guidance

Rather than forcing the quadcopter to be at a specific coordinate at a specific timestamp, the geometric vector field (VF) approach creates a spatial map of unit course directions that drive the quadcopter to converge onto the scanning orbit path while maintaining velocity using PI velocity controller [24].

Let the distance to the tower center (x_t, y_t) be $d(t) = \sqrt{(x-x_t)^2 + (y-y_t)^2}$, and the radial distance error be $\hat{d}(t) = d(t) - R$. The current phase angle of the quadrotor relative to the tower is defined as:

$$\gamma(t) = \text{atan2}(y - y_t, x - x_t) \tag{31}$$

The commanded course angle χ_{cmd} is generated based on the radial path error [11]:

$$\chi_{cmd}(t) = \gamma(t) + \lambda\left(\frac{\pi}{2} + \tan^{-1}\left(k_0 \hat{d}(t)\right)\right) \tag{32}$$

Where $\lambda \in \{-1, +1\}$ determines the orbit direction (clockwise or counterclockwise), and $k_0 > 0$ is a convergence gain that governs the entry profile.

As $\hat{d} \to \infty$, $\tan^{-1}(k_0\hat{d}) \to \pi/2$, commanding the quadrotor to fly directly toward the center of the tower. When the vehicle is on the orbit boundary $(\hat{d} = 0)$, $\tan^{-1}(0) = 0$, aligning the commanded course perfectly tangent $(\gamma + \lambda\pi/2)$ to the circle.

Then, the horizontal reference velocities are computed using the desired ground scan speed V_d ($V_d = R\omega_0 =$ 1.5 m/s, so that all guidance laws scan at the same rate) and passed as inputs to the velocity tracking loops:

$$v_{x,d}(t) = V_d \cos(\chi_{cmd}(t)) \tag{33}$$

$$v_{y,d}(t) = V_d \sin(\chi_{cmd}(t)) \tag{34}$$

2.3.3 Convergence Analysis of the Vector Field

Assume first that the velocity loop tracks its reference exactly, so that the horizontal ground velocity equals $V_d[\cos(\chi_{cmd}),\ \sin(\chi_{cmd})]^T$. Using (32) and $\cos\left(\lambda\left(\frac{\pi}{2}+a\right)\right) = -\sin(a)$, the radial distance evolves as

$$\dot{d} = V_d\cos(\chi_{cmd}-\gamma) = -\frac{V_d k_0 \hat{d}}{\sqrt{1+k_0^2\hat{d}^2}} \tag{35}$$

With the Lyapunov candidate $W = 1/2\ \hat{d}^2$,

$$\dot{W} = \hat{d}\,\dot{d} = -\frac{V_d k_0 \hat{d}^2}{\sqrt{1+k_0^2\hat{d}^2}} < 0, \quad \forall\,\hat{d}\neq 0 \tag{36}$$

so the orbit $\hat{d}=0$ is asymptotically stable for every initial position except the tower center ($d=0$), where γ is undefined. Near the orbit $\dot{d}\approx -V_d k_0 \hat{d}$, i.e. the convergence is exponential with time constant $\tau = 1/(V_d k_0)$, whereas far from the orbit the approach speed saturates at V_d. On the orbit the phase rate is $\dot{\gamma} = \lambda V_d/R$, so choosing $V_d = R\omega_0$ gives the same scan rate as the time-parameterized reference (26)–(28). Now let the velocity loop have a tracking error $\varepsilon(t)$ caused by gusts, turbulence, and loop dynamics, with radial component $|\varepsilon_r| \le \varepsilon_{max} < V_d$. Then

$$\dot{W} \le -|\hat{d}|\left(\frac{V_d k_0|\hat{d}|}{\sqrt{1+k_0^2\hat{d}^2}} - \varepsilon_{max}\right) \tag{37}$$

which is negative whenever $|\hat{d}|$ exceeds

$$d_{ub} = \frac{\varepsilon_{max}}{k_0\sqrt{V_d^2-\varepsilon_{max}^2}} \tag{38}$$

Hence $\hat{d}$ is uniformly ultimately bounded after any time t_0, $|\hat{d}(t)| \le \max(|\hat{d}(t_0)|, d_{ub})$. Because the integral terms of (22)–(23) remove the constant part of the wind disturbance, ε_{max} reflects only its time-varying part. The analysis treats the velocity loop as a faster inner loop (time-scale separation). A complete proof for the full cascade including the attitude dynamics is beyond the scope of this paper. The bound is verified numerically in Section 3.3.

2.3.4 NLGL Baseline

As a baseline from the literature, the nonlinear guidance logic (NLGL) of Park et al. [23] is adapted to the orbit. A reference point is placed on the orbit at distance L_1 ahead of the vehicle (or at the closest orbit point when the orbit is farther than L_1), and η is the angle between the commanded course χ_d and the line of sight to that point. The NLGL lateral acceleration $a_{lat} = \frac{2V_d^2\sin(\eta)}{L_1}$ is converted into a course-rate command, as on the fixed-wing platform for which NLGL was designed,

$$\dot{\chi}_d = \frac{a_{lat}}{V_d} = \frac{2V_d\sin(\eta)}{L_1} \tag{39}$$

and the resulting velocity reference

$$v_{x,d} = V_d\cos(\chi_d), \qquad v_{y,d} = V_d\sin(\chi_d) \tag{40}$$

is tracked by the same velocity PI loop (22)–(23) as the proposed method, so that NLGL and the VF differ only in the guidance law.

2.4 Active Yaw "Gaze-Locking" Control

For high-fidelity 3D photogrammetric reconstruction, the vehicle's onboard camera, mounted on a two-axis gimbal that compensates roll and pitch, is aligned in yaw with the $+X_B$ body axis and must remain oriented

orthogonally toward the central scanning axis [2],[18]. To maintain this gaze-lock on the tower center (x_t, y_t), the yaw command (ψ_d) is updated dynamically based on real-time positional coordinates:

$$\psi_d(t) = \text{atan2}\big(y_t - y(t), x_t - x(t)\big) \tag{41}$$

Since the physical position is continuously shifting due to orbital movement and wind drift, the yaw tracking error $e_\psi = \psi_d(t) - \psi(t)$ is normalized within the range $[-\pi, \pi]$ to avoid trigonometric wrap-around spikes:

$$e_{\psi,normalized} = \text{mod}\big(e_\psi + \pi, 2\pi\big) - \pi \tag{42}$$

This continuous gaze steering ensures that the tower remains centered on the optical sensor, eliminating target clipping and maintaining structural feature overlap between sequential video frames.

The camera is modeled as a pinhole camera with a 36 mm × 24 mm sensor, a 35 mm focal length, and an image width of $W = 4000$ px, which gives a horizontal field of view $\text{HFoV} = 2\tan^{-1}(s_w/2f) = 54.4°$. A yaw pointing error e_ψ shifts the tower axis in the image by

$$\Delta u = f_{px}\tan(e_\psi), \qquad f_{px} = \frac{W/2}{\tan(\text{HFoV}/2)} \approx 3889 \text{ px} \tag{43}$$

At the 10 m stand-off distance the frame spans 10.3 m horizontally. Because the camera is gimbal-stabilized in roll and pitch, the horizontal pointing error equals the yaw error. For a camera rigidly fixed to the body, the steady tilt into the wind adds a further pointing error, which is reported separately in Section 3.4.

2.5 Simulation Environment and Wind Configuration

The evaluation of all controllers is performed using a continuous-time simulation environment implemented in Python, execution at a fixed step-size of $2\ ms$ (500 Hz) to model the high-fidelity flight dynamics. All integrators are clamped to prevent wind-up: ±2 m·s for the position and altitude integrals, ±5 m for the velocity integrals, and ±1 rad·s for the attitude integrals.

The vehicle is subjected to a realistic compound aerodynamic model. The total drag force acting on the quadcopter frame is proportional to its translational velocity relative to the local wind velocity:

$$\mathbf{F}_{drag} = m\, c_d(\mathbf{v} - \mathbf{v}_{wind}) \tag{44}$$

Where $c_d = 0.25\ \text{s}^{-1}$ is the linear drag coefficient per unit mass.

The simulated wind vector consists of three components,

$$\mathbf{v}_{wind}(t) = \mathbf{v}_{mean} + \mathbf{v}_g(t) + \mathbf{v}_{turb}(t) \tag{45}$$

- Steady Mean Crosswind: A constant $4.5\ \text{m/s}$ wind coming from a 45^o azimuth (North-East), i.e. blowing toward the south-west; in the Monte Carlo study of Section 3.3 the direction is drawn uniformly from [0°, 360°).
- Dynamic Gusts: A low-frequency sinusoidal drift $v_{gust}(t) = 1.5\sin(0.2t)\ \text{m/s}$ along the mean wind direction.
- Turbulence: the Dryden continuous turbulence model in the low-altitude form of MIL-HDBK-1797 [25], generated by passing unit-variance white noise through the forming filters

$$H_u(s) = \sigma_u\sqrt{\frac{2L_u}{\pi V}}\,\frac{1}{1 + \frac{L_u}{V}s} \tag{46}$$

$$H_v(s) = \sigma_v\sqrt{\frac{2L_v}{\pi V}}\,\frac{1 + 2\sqrt{3}\frac{L_v}{V}s}{\left(1 + 2\frac{L_v}{V}s\right)^2} \tag{47}$$

and H_w has the same structure as H_v, using L_w and σ_w. Below 1000 ft, with h in ft,

$$L_u = 2L_v = \frac{h}{(0.177 + 0.000823h)^{1.2}}, \qquad 2L_w = h \tag{48}$$

$$\sigma_w = 0.1W_{20}, \qquad \sigma_u = \sigma_v = \frac{\sigma_w}{(0.177 + 0.000823h)^{0.4}} \tag{49}$$

where W_{20} is the wind speed at 20 ft (6 m). Because the airspeed of the quadcopter during the orbit is small, the mean wind speed is used as the advection speed V (frozen-turbulence assumption). We use $W_{20} = 4.5$ m/s and evaluate the scales at the reference altitude of the helix (with $h \geq 10$ ft), which gives $\sigma_u = \sigma_v$ from 0.88 to 0.72 m/s and $\sigma_w = 0.45$ m/s over the 2–50 m altitude range. The turbulence components act along the mean wind (u), across it (v), and vertically (w).

To test the robust convergence of the controllers, the quadcopter is initialized at a significant offset location $\boldsymbol{p}_0 = [12, -2, 0]^T$ m, placing it outside the desired scanning orbit, and is commanded to ascend and lock into the 10-meter orbit radius. Each run lasts 120 s (about 2.9 orbits), during which the vehicle climbs from 2 m to 50 m.

3 Results and Discussion

To evaluate the performance of the proposed Geometric Vector Field (VF) guidance law against classical cascaded Proportional-Integral-Derivative (PID) trajectory tracking and the NLGL baseline, a series of continuous-time numerical simulations were carried out under identical, severe environmental conditions. The simulations model the quadcopter performing a 3D helical scan of a tall structure (tower) located at coordinate $(0,0,0)$ with a target radius $R = 10\,m$, a slow climb rate of $0.4\,m/s$, and an orbital speed of $0.15\,rad/s$. The quadcopter is launched from a significant initial offset coordinate $(12, -2, 0)$ to test the entry and convergence characteristics of all flight algorithms.

The cascaded inner-outer loop controllers gains are shared by all controllers as shown in Table 1.

Table 1. Inner-outer loop control parameters

No.	Control Parameters	Description	Value
1	$K_{P\phi}, K_{P\theta}$	Proportional gain on attitude and rate	8.0
2	$K_{I\phi}, K_{I\theta}$	Integral gain on attitude and rate	0.01
3	$K_{D\phi}, K_{D\theta}$	Derivative gain on attitude and rate	0.8
4	$K_{P\psi}$	Proportional gain on the yaw control	6
5	$K_{I\psi}$	Integral gain on the yaw control	0.01
6	$K_{D\psi}$	Derivative gain on the yaw control	0.6
7	K_{Pz}	Proportional gain on the altitude tracker	10
8	K_{Iz}	Integral gain on the altitude tracker	0.1
9	K_{Dz}	Derivative gain on the altitude tracker	5

3.1 Transient Performance and Orbit Convergence

The transient response represents a critical flight phase where the vehicle transitions from free positioning to a stable loitering manifold. Under calm conditions, all controllers successfully guide the quadrotor to the starting altitude of $z = 2\,m$ and onto the $10\,m$ radius circle. However, their transient trajectories exhibit distinct behaviours when subjected to identical initial conditions. All controllers were tuned with a global-best particle swarm optimization (PSO) using the same evaluation budget. Each particle position contains the three outer-loop parameters of one controller, and its cost is the RMS of the radial error $\hat{d}$ over a 60 s run, averaged over three wind realizations (Section 2.5) whose seeds are not reused in the evaluation runs of Section 3.3. The PSO settings and search bounds are listed in Table 3 and the resulting gains in Table 2. Several gains reached the limits of the search space; these limits keep the outer loops at least about 2.5 times slower than the attitude loop, whose natural frequency is about 27 rad/s. Because the simulation contains no position-sensor noise, higher gains are not penalized, so the absolute errors reported below should be read as lower bounds.

Table 2. PSO-optimized outer-loop parameters

No.	Control parameters	Description	Value
PID position control trajectory tracking			
1	K_{Ppos}	Proportional gain on Position control	10.0
2	K_{Ipos}	Integral gain on Position control	4.28
3	K_{Dpos}	Derivative gain on Position control	7.31
PI velocity control geometric vector field			
1	k_0	Transition rate gain to orbit path	2.00
2	K_{Pv}	Velocity error gain	5.45
3	K_{Iv}	Velocity integral gain (rejects wind drift)	5.00
NLGL baseline [22] with the velocity PI loop of (22)–(23)			
1	L_1	Look-ahead distance (m)	1.00
2	K_{Pv}	Velocity error gain	7.16
3	K_{Iv}	Velocity integral gain (rejects wind drift)	5.00

Table 3. PSO settings and search bounds

No.	Symbol	Setting	Value
1	n_p	Swarm size	30
2	n_{it}	Iterations	20
3	w	Inertia weight	0.4
4	c_1	Cognitive coefficient	1.7
5	c_2	Social coefficient	1.7
6	v_{max}	Particle velocity limit	20% of search range
7	J	Cost: RMS of $\hat{d}$ over 60 s, mean of 3 tuning winds	–
8	–	Bounds, PID (K_{Ppos}, K_{Ipos}, K_{Dpos})	[0, 10], [0, 5], [0, 10]
9	–	Bounds, VF (k_0, K_{Pv}, K_{Iv})	[0.05, 2], [0.1, 10], [0, 5]
10	–	Bounds, NLGL (L_1 in m, K_{Pv}, K_{Iv})	[1, 19], [0.1, 10], [0, 5]

The standard trajectory tracker commands coordinate relative to a moving temporal clock, $\mathbf{p}_d(t)$. Because the quadcopter is launched from an initial distance offset of approximately 2.8 m from the reference start coordinates, the standard controller generates high virtual acceleration demands to catch up with the moving virtual point on the path. This results in an overshoot of 0.27 m inside the orbit at $t \approx 1.4$ s for the PID tracker (0.28 m at $t \approx 2.0$ s for NLGL), whereas the VF enters the orbit without overshoot and settles within ±0.25 m after 1.4 s, as shown in Figure 2.

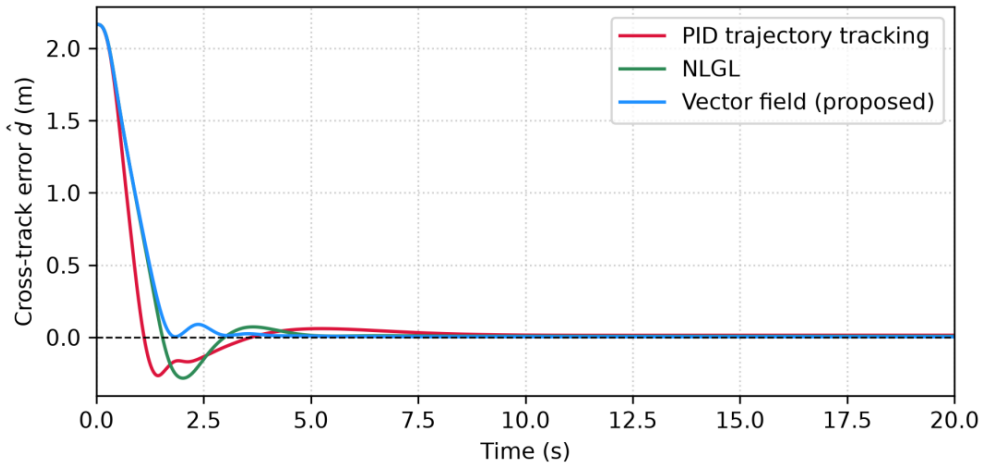


Figure 2. Cross-track error comparison: no wind ($d_{curr} - R_{orbit}$)

In contrast, the Geometric Vector Field guidance law commands course headings χ_{cmd} based purely on spatial distance from the orbit path boundary, completely removing any time dependence. As illustrated in the top-view flight profile, see Figure 3 , the VF controller guides the quadrotor along a highly smooth, direct asymptotic curve the merges into the orbit path seamlessly without the prominent initial oscillations typical of time-constrained trackers. After convergence in calm air, the residual radial error is 15 mm for PID, 8 mm for NLGL, and 4 mm for the VF; these residuals arise because none of the outer loops includes a centripetal acceleration feed-forward.

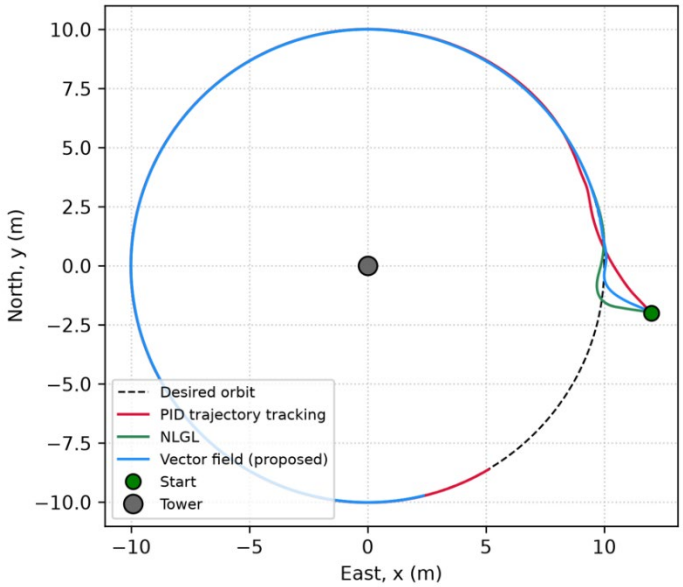
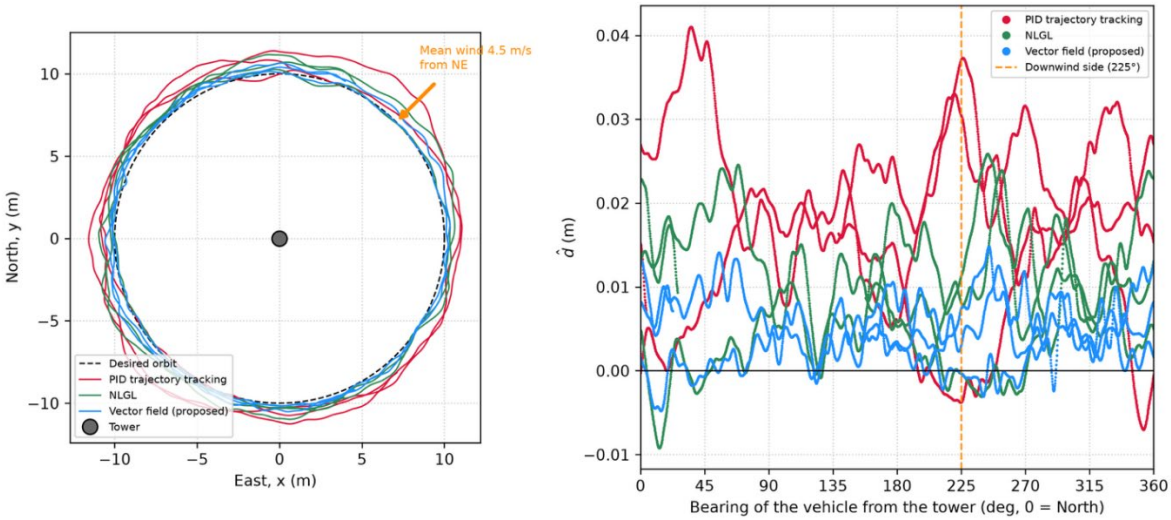


Figure 3. Top-down orbit paths

3.2 Trajectory Tracking in Wind Disturbances

The primary objective of the simulation was to assess the disturbance rejection capability on typical outdoor atmospheric conditions at working altitude of (10 - 50 m) near tall structures such as towers. Hence, all control loops are exposed to a 4.5 m/s mean wind from the north-east (45° azimuth, which couples both horizontal axes along the circular orbit), a sinusoidal gust of ±1.5 m/s, and Dryden turbulence. The results for a representative wind realization (turbulence seed 0) are shown in Figure 4.

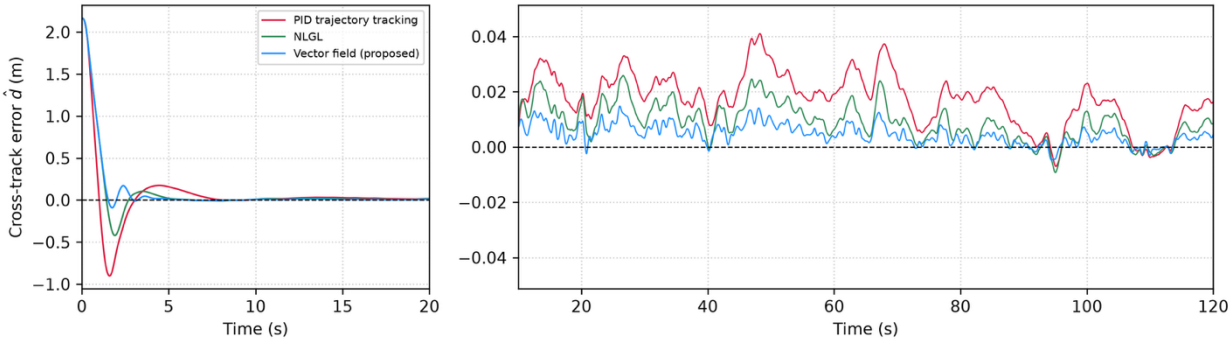


(a) (b)

Figure 4. Top-Down Orbit Paths under Wind Drift: (a) orbit shape with magnified radial deviation, (b) radial deviation around the orbit

Under wind, all three controllers remain on the orbit to within a few centimeters once the entry transient has decayed (Figure 4 and Figure 5b). The radial error is mostly positive, i.e. the vehicle flies slightly outside the

orbit, because none of the outer loops includes a centripetal acceleration feed-forward; superimposed on this offset are fluctuations driven by the gusts and the Dryden turbulence. The time-parameterized PID tracker shows the largest deviations, up to 41 mm in this realization, because the wind delays the vehicle with respect to its moving reference point and the controller must correct a spatial and a temporal error at the same time. Variations of the radial error change the camera-to-tower distance and therefore the ground sampling distance (GSD) of the images, which is relevant for 3D reconstruction.



(a) (b)

Figure 5. Cross-Track Error Comparison $(d_{curr} - R_{orbit})$ under wind: (a) entry transient, (b) after convergence (zoomed)

The VF guidance law keeps the smallest deviation, with a maximum of 15 mm after convergence in this realization (26 mm for NLGL). Because the VF commands course directions that bend toward the orbit based on the actual radial offset, it does not have to resynchronize with a moving reference, and because its commands are tracked by the velocity PI loop, the integral action estimates the steady part of the wind force and tilts the vehicle into the wind (a mean tilt of about 7.6° in this realization) while the ground course stays on the circle. During the entry transient under wind, the PID tracker overshoots 0.90 m inside the orbit, NLGL 0.42 m, and the VF 0.09 m (Figure 5a).

3.3 Quantitative Performance Comparison

To assess statistical significance, each controller was evaluated in N = 30 paired Monte Carlo runs. In run i all controllers experience the same wind realization: the mean wind direction is drawn uniformly from [0°, 360°) and the Dryden turbulence uses noise seed i. Each run lasts 120 s, and the metrics are computed after $t = 10$ s to exclude the initial convergence. Table 4 reports the mean ± standard deviation over the runs, and the differences were tested with a two-sided Wilcoxon signed-rank test on the paired runs ($\alpha = 0.05$). Figure 6 shows the distributions of the main metrics.

Table 4. Monte Carlo performance metrics under wind (mean ± SD over N = 30 paired runs)

Performance metric	PID	NLGL [22]	VF (proposed)	Reduction vs PID	Reduction vs NLGL
Mean cross-track error (mm)	15.32 ± 1.11	8.72 ± 0.58	4.51 ± 0.28	70.6%*	48.3%*
Maximum cross-track error (mm)	36.87 ± 4.72	24.97 ± 3.22	14.01 ± 1.90	62.0%*	43.9%*
Stand-off distance SD (mm)	10.48 ± 1.22	6.69 ± 0.51	3.59 ± 0.25	65.8%*	46.4%*
Mean altitude tracking error (mm)	15.19 ± 2.57	15.54 ± 2.62	15.52 ± 2.62	−2.2%*	0.1%
Mean yaw pointing error (deg)	0.794 ± 0.009	0.791 ± 0.007	0.786 ± 0.002	1.0%*	0.7%*
Maximum yaw pointing error (deg)	0.867 ± 0.014	0.862 ± 0.014	0.853 ± 0.007	1.5%*	1.0%*
Maximum image-plane offset (px)	58.8 ± 1.0	58.5 ± 1.0	57.9 ± 0.5	1.5%*	1.0%*
Mean pointing error, body-fixed camera (deg)	4.44 ± 0.48	4.45 ± 0.47	4.45 ± 0.47	−0.2%	0.1%
Roll/pitch command rate RMS (rad/s)	0.022 ± 0.001	0.021 ± 0.001	0.022 ± 0.001	0.0%	−4.4%*

*Reduction = 1 − VF/baseline (positive: VF lower). * p < 0.001, two-sided Wilcoxon signed-rank test on the 30 paired runs.*

The VF guidance law reduces the mean cross-track error by 70.6% relative to PID trajectory tracking (from 15.3 mm to 4.5 mm) and by 48.3% relative to NLGL, and it reduces the stand-off distance variation, which determines the GSD consistency of the images, by 65.8% and 46.4%, respectively (all $p < 0.001$). The improvement over NLGL, which uses the same velocity PI loop, isolates the contribution of the guidance law itself. The absolute errors are small for all controllers because the PSO drove the outer-loop gains to the limits of the search space in a simulation without sensor noise; with the earlier manually tuned gains (PID 1.5/0.01/1.8, VF 0.3/3.0/0.5), the same Monte Carlo study gives mean cross-track errors of 0.481 m and 0.206 m (−57.2%), so the ranking does not depend on the tuning. The mean altitude tracking error is practically identical for all controllers (15.2–15.5 mm): the proposed method changes only the horizontal guidance, all configurations share the same altitude loop (8) and climb reference (28), and the vertical channel is disturbed mainly through attitude coupling and vertical turbulence, which are the same for all controllers. Likewise, the roll/pitch command rate, a measure of actuator jitter, does not differ between the VF and PID.

For the VF, the largest radial velocity-tracking error after $t = 20$ s was $\varepsilon_{max} = 0.046 \pm 0.005$ m/s, which gives $d_{ub} = 15.5 \pm 1.7$ mm from (38). The observed maximum radial error over the same window, 13.1 ± 1.5 mm, remained below d_{ub} in all 30 runs, which confirms the ultimate bound of Section 2.3.3.

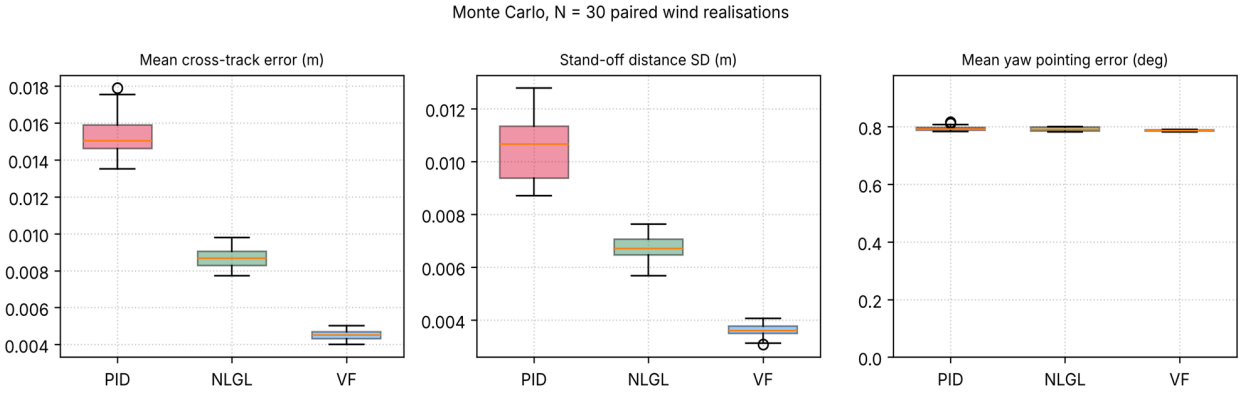


Figure 6. Monte Carlo distributions (N = 30 paired runs) of the mean cross-track error, the stand-off distance standard deviation, and the mean yaw pointing error

3.4 Camera Pointing and Photogrammetry Implications

For high-altitude 3D photogrammetric reconstruction, maintaining the target structure at the exact center of the camera's optical frame is as critical as keeping the vehicle on its flight path. Any rapid oscillations or tracking drifts in yaw can lead to rotational image blur, target clipping, and poor overlapping sequences, which severely degrade the subsequent structure-from-motion (SfM) feature matching algorithms.

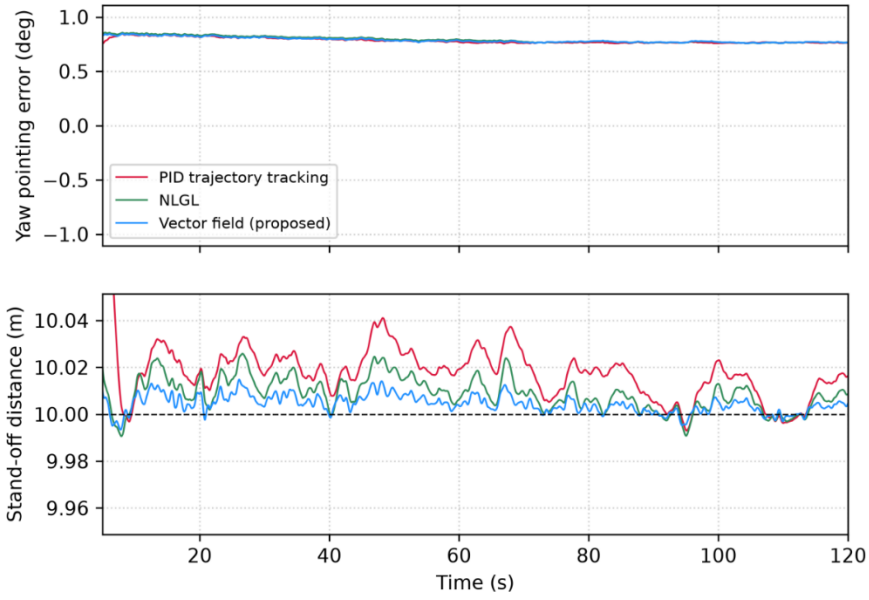


Figure 7. Yaw pointing error and stand-off distance in the representative wind realization

Figure 7 shows the yaw pointing error and the stand-off distance in the representative realization. In contrast to the path errors, the pointing error is practically the same for all controllers: about 0.79° on average and below 0.87° at its maximum (Table 4). The gaze-locking law (41) computes the yaw reference from the measured position, so a path deviation changes the reference but does not create a pointing error; the residual error is the lag of the yaw loop as the line of sight rotates at the orbital rate ω_0. With the camera model of Section 2.4, a 0.87° error shifts the tower axis by about 59 px, or 1.5% of the image width, which is far from clipping the tower out of the 10.3 m wide frame. For a camera rigidly fixed to the body, the tilt into the wind (about 7.6° on average) dominates instead and produces a mean pointing error of 4.4° for every controller, which motivates the gimbal assumption of Section 2.4.

Figure 8 shows the 3D helical paths under wind; the orange arrows are the camera optical axes of the VF controller, plotted every 2 s, and remain directed at the tower axis throughout the climb. The benefit of the VF for photogrammetry is therefore not a better pointing accuracy but a more constant camera-to-tower distance, and thus a more uniform GSD and image overlap, while the pointing accuracy is preserved by the decoupled yaw loop.

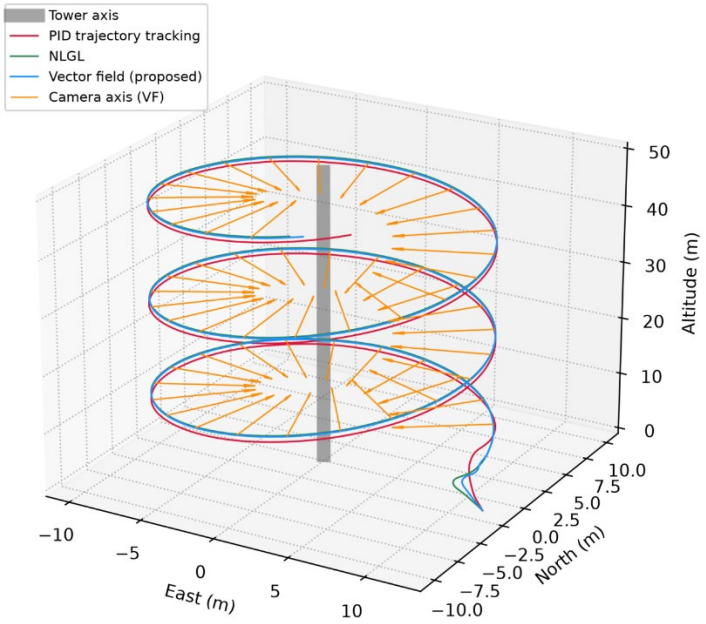


Figure 8. 3D helical scan under wind; the orange arrows show the camera optical axis of the VF controller every 2 s

3.5 Discussion on Physical Rejection Mechanisms

The physical reason for the lower path error of the Geometric Vector Field controller lies in its time-decoupled guidance formulation. In a standard trajectory tracking structure, a reference specified in time is tracked, where the references of the path are given by a temporal evolution of each space coordinate. Under external wind forces, the vehicle is pushed away from the reference coordinate, generating a spatial tracking error and a temporal phase-lag. The PID loop tries to correct both simultaneously, leading to overshoot during the entry and larger residual deviations.

By removing time-dependence, the Vector Field guidance law defines a stable manifold in space. The set of vectors is virtually placed around the path in such a way that if the vehicle follows the direction of those vectors it will converge to the path, generating desired course inputs to the lower-level controller. Once close to the path, the controller focuses exclusively on keeping the cross-track error to zero, permitting the forward ground speed to vary naturally to counteract headwind or tailwind components.

Furthermore, by translating the spatial vector field commands into desired ground velocity target (v_{xd}, v_{yd}) rather than direct attitude tilt angles, the guidance system leverages a hierarchical, cascading velocity control architecture. Under persistent crosswind conditions, the integral component of the outer-loop velocity PI controller $(\int e_v d\tau)$ functions as a passive aerodynamic force estimator. Because aerodynamic drag $(\mathbf{F}_{drag})$ retards the quadcopter's lateral motion, the velocity error integral continuously accumulates and stores the unmeasured aerodynamic force offset. In accordance with the internal model principle in control theory, this accumulation continues until the virtual acceleration demands generate a control force that precisely balances the steady-state wind drag $(m \cdot u_{acc,integral} \approx -\mathbf{F}_{drag,wind})$. Consequently, the system implicitly reconstructs

and counteracts external wind forces in real time without requiring additional physical sensors, such as pitot tubes or onboard anemometers.

This implicit force estimation translates directly into physical tilt demands (ϕ_d, θ_d), enabling an automatic, coordinated crab maneuver or wind correction angle. By maintaining a steady-state roll and pitch tilt into the oncoming wind vector, a horizontal component of the quadcopter's rotor thrust is redirected to cancel out lateral atmospheric drift, maintaining a precise ground path along the circular orbit boundary. Crucially, because translational wind rejection is handled entirely through roll and pitch body tilts via the velocity integral, the vehicle's yaw heading (ψ) is completely decoupled from path-following guidance. This structural decoupling allows the active gaze-locking controller to independently steer the camera's optical axis directly toward the central axis of the object without compromising aerodynamic drift compensation. The Monte Carlo results confirm this decoupling: the pointing error is the same for all three guidance laws, whereas the path and stand-off errors differ significantly.

4 Conclusion

This paper presents a robust cascaded control system integrating Geometric Vector Field (VF) guidance with active Gaze-Locking yaw control to enable precise, close-range 3D helical scanning of tall structures under aerodynamic disturbances. By decoupling spatial convergence from temporal constraints, the time-independent VF controller allows the vehicle to focus its control authority exclusively on path convergence rather than adhering for rigid temporal schedules. Comparative 6-DoF continuous-time simulating studies under a challenging aerodynamic profile (consisting of a 4.5 m/s mean wind, sinusoidal gusts, and Dryden turbulence) show that the proposed method significantly outperforms a time-parameterized PID tracker and the NLGL baseline in path accuracy.

Over 30 paired Monte Carlo runs with PSO-tuned gains, the VF reduced the mean cross-track error from 15.3 mm (PID) and 8.7 mm (NLGL) to 4.5 mm, i.e. by 70.6% and 48.3%, and reduced the stand-off distance variation by 65.8% and 46.4% ($p < 0.001$). The camera pointing error, in contrast, was about 0.8° (below 60 px) for all guidance laws, because the gaze-locking law uses the measured position and is decoupled from path following; a gimbal is needed to keep the tilt into the wind out of the camera line of sight. A Lyapunov analysis gives asymptotic convergence of the vector field and an ultimate bound on the radial error that was satisfied in all runs. These findings show that geometric path-following guidance with a cascaded velocity loop compensates wind passively through coordinated crab angles, and that its main benefit for photogrammetry is a more constant stand-off distance rather than better pointing.

For future work, the authors recommend validating the mathematical formulations and control loops on physical quadrotor hardware, such as an open-source PX4 or Ardupilot research platform, in outdoor test facilities, together with position-sensor noise and latency, which limit the achievable outer-loop gains. Additionally, exploring the scaling of this geometric vector field framework to accommodate multi-UAV cooperative scanning configurations would be highly beneficial. This would allow a decentralized swarm of autonomous agents to divide a single structure into multiple synchronized altitude sectors, accelerating the data collection process while maintaining tight inter-agent separation distances and robust collision avoidance in turbulent wind environments.

Acknowledgement

This research was done autonomously without being funded by any institution.

Reference

[1] V. V. An, T. L. Mien, and N. V. Binh, "A comprehensive survey of UAV control algorithms: Integrating classical methods with artificial intelligence for enhanced trajectory tracking," *AIMS Electron. Electr. Eng.*, vol. 10, no. 1, pp. 26–53, 2026. https://doi.org/10.3934/electreng.2026002

[2] F. Nex *et al.*, "UAV in the advent of the twenties: Where we stand and what is next," *ISPRS J. Photogramm. Remote Sens.*, vol. 184, pp. 215–242, Feb. 2022. https://doi.org/10.1016/j.isprsjprs.2021.12.006

[3] C. V. Nguyen, M. T. Nguyen, H. T. Tran, M. L. Trinh, H. M. La, and H. T. T. Nguyen, "Trajectory Tracking Control for a Quadcopter under External Disturbances," *Eng. Technol. Appl. Sci. Res.*, vol. 14, no. 6, pp. 17620–17628, 2024. https://doi.org/10.48084/etasr.8449

[4] Y. Alshawabkeh, A. Baik, and A. Fallatah, "As-Textured As-Built BIM Using Sensor Fusion, Zee Ain Historical Village as a Case Study," *Remote Sens.*, vol. 13, no. 24, p. 5135, Dec. 2021. https://doi.org/10.3390/rs13245135ht

[5] M. Navabi and H. Mirzaei, "Robust Optimal Adaptive Trajectory Tracking Control of Quadrotor Helicopter," *Lat. Am. J. Solids Struct.*, vol. 14, no. 6, pp. 1040–1063, Jun. 2017. https://doi.org/10.1590/1679-78253595
[6] B. Rubí, R. Pérez, and B. Morcego, "A Survey of Path Following Control Strategies for UAVs Focused on Quadrotors," *J. Intell. Robot. Syst.*, vol. 98, no. 2, pp. 241–265, May 2020. https://doi.org/10.1007/s10846-019-01085-z
[7] F. Zhu *et al.*, "Swarm-LIO2: Decentralized Efficient LiDAR-Inertial Odometry for Aerial Swarm Systems," *IEEE Trans. Robot.*, vol. 41, pp. 960–981, 2025. https://doi.org/10.1109/TRO.2024.3522155
[8] A. Baharuddin and M. A. Mohd Basri, "Trajectory Tracking of a Quadcopter UAV using PID Controller," *Elektr.- J. Electr. Eng.*, vol. 22, no. 2, pp. 14–21, Aug. 2023. https://doi.org/10.11113/elektrika.v22n2.440h
[9] A. Maji, "Learning model predictive control with application to quadcopter trajectory tracking," Master's Thesis, KTH Royal Institute of Technology, Sweden, 2023. [Online]. Available: https://www.diva-portal.org/1453324
[10] B. Li *et al.*, "Multi-UAV Trajectory Planning during Cooperative Tracking Based on a Fusion Algorithm Integrating MPC and Standoff," *Drones*, vol. 7, no. 3, p. 196, Mar. 2023. https://doi.org/10.3390/drones7030196
[11] D. R. Nelson, D. B. Barber, T. W. McLain, and R. W. Beard, "Vector Field Path Following for Miniature Air Vehicles," *IEEE Trans. Robot.*, vol. 23, no. 3, pp. 519–529, Jun. 2007. https://doi.org/10.1109/TRO.2007.898976
[12] Y. A. Kapitanyuk, A. V. Proskurnikov, and M. Cao, "A Guiding Vector-Field Algorithm for Path-Following Control of Nonholonomic Mobile Robots," *IEEE Trans. Control Syst. Technol.*, vol. 26, no. 4, pp. 1372–1385, Jul. 2018. https://doi.org/10.1109/TCST.2017.2705059
[13] V. M. Goncalves, L. C. A. Pimenta, C. A. Maia, B. C. O. Dutra, and G. A. S. Pereira, "Vector Fields for Robot Navigation Along Time-Varying Curves in n-Dimensions," *IEEE Trans. Robot.*, vol. 26, no. 4, pp. 647–659, Aug. 2010. https://doi.org/10.1109/TRO.2010.2053077
[14] X. Wang, S. Baldi, X. Feng, C. Wu, H. Xie, and B. De Schutter, "A Fixed-Wing UAV Formation Algorithm Based on Vector Field Guidance," *IEEE Trans. Autom. Sci. Eng.*, vol. 20, no. 1, pp. 179–192, Jan. 2023. https://doi.org/10.1109/TASE.2022.3144672
[15] Z. Wang and Y. Luo, "Elliptical Multi-Orbit Circumnavigation Control of UAVS in Three-Dimensional Space Depending on Angle Information Only," *Drones*, vol. 6, no. 10, p. 296, Oct. 2022. https://doi.org/10.3390/drones6100296
[16] D. A. Lawrence, E. W. Frew, and W. J. Pisano, "Lyapunov Vector Fields for Autonomous Unmanned Aircraft Flight Control," *J. Guid. Control Dyn.*, vol. 31, no. 5, pp. 1220–1229, Sep. 2008. https://doi.org/10.2514/1.34896
[17] E. M. Lee *et al.*, "CEO-MLCPP: Control-Efficient and Obstacle-Aware Multi-Layer Coverage Path Planner for 3D Reconstruction with UAVs," in *Robot Intelligence Technology and Applications 7*, vol. 642, J. Jo, H.-L. Choi, M. Helbig, H. Oh, J. Hwangbo, C.-H. Lee, and B. Stantic, Eds., in Lecture Notes in Networks and Systems, vol. 642. , Cham: Springer International Publishing, 2023, pp. 27–36. https://doi.org/10.1007/978-3-031-26889-2_3
[18] S. Zhang, C. Liu, and N. Haala, "Guided by model quality: UAV path planning for complete and precise 3D reconstruction of complex buildings," *Int. J. Appl. Earth Obs. Geoinformation*, vol. 127, p. 103667, Mar. 2024. https://doi.org/10.1016/j.jag.2024.103667
[19] F. Nex and F. Remondino, "UAV for 3D mapping applications: a review," *Appl. Geomat.*, vol. 6, no. 1, pp. 1–15, Mar. 2014. https://doi.org/10.1007/s12518-013-0120-x
[20] R. Rysdyk, "Unmanned Aerial Vehicle Path Following for Target Observation in Wind," *J. Guid. Control Dyn.*, vol. 29, no. 5, pp. 1092–1100, Sep. 2006. https://doi.org/10.2514/1.19101
[21] E. W. Frew, D. A. Lawrence, and S. Morris, "Coordinated Standoff Tracking of Moving Targets Using Lyapunov Guidance Vector Fields," *J. Guid. Control Dyn.*, vol. 31, no. 2, pp. 290–306, Mar. 2008. https://doi.org/10.2514/1.30507
[22] P. B. Sujit, S. Saripalli, and J. B. Sousa, "Unmanned Aerial Vehicle Path Following: A Survey and Analysis of Algorithms for Fixed-Wing Unmanned Aerial Vehicless," *IEEE Control Syst. Mag.*, vol. 34, no. 1, pp. 42–59, Feb. 2014. https://doi.org/10.1109/MCS.2013.2287568
[23] S. Park, J. Deyst, and J. P. How, "Performance and Lyapunov Stability of a Nonlinear Path Following Guidance Method," *J. Guid. Control Dyn.*, vol. 30, no. 6, pp. 1718–1728, Nov. 2007. https://doi.org/10.2514/1.28957
[24] A. Shivam and A. Ratnoo, "Arcsine Vector Field for Path Following Guidance," *J. Guid. Control Dyn.*, vol. 46, no. 12, pp. 2409–2420, Dec. 2023. https://doi.org/10.2514/1.G007562
[25] U.S. Departement of Defence, *Flying Qualities of Piloted Aircraft, MIL-HDBK-1797*. 1997.